ACS APPLIED MATERIALS & INTERFACES

Research Article

www.acsami.org

Enhancing the Oxygen Permeation Rate of $Zr_{0.84}Y_{0.16}O_{1.92}$–$La_{0.8}Sr_{0.2}Cr_{0.5}Fe_{0.5}O_{3-\delta}$ Dual-Phase Hollow Fiber Membrane by Coating with $Ce_{0.8}Sm_{0.2}O_{1.9}$ Nanoparticles

Tong Liu,[†] Yao Wang,[†] Ronghua Yuan,[†] Jianfeng Gao,[†] Chusheng Chen,*[,†] and Henny J.M. Bouwmeester*[,‡]

[†]CAS Key Laboratory of Materials for Energy Conversion, Department of Materials Science and Engineering, University of Science and Technology of China, Hefei 230026, China

[‡]Inorganic Membranes, Department of Science and Technology, and MESA+ Institute for Nanotechnology, University of Twente, P.O. Box 217, 7500 AE Enschede, The Netherlands

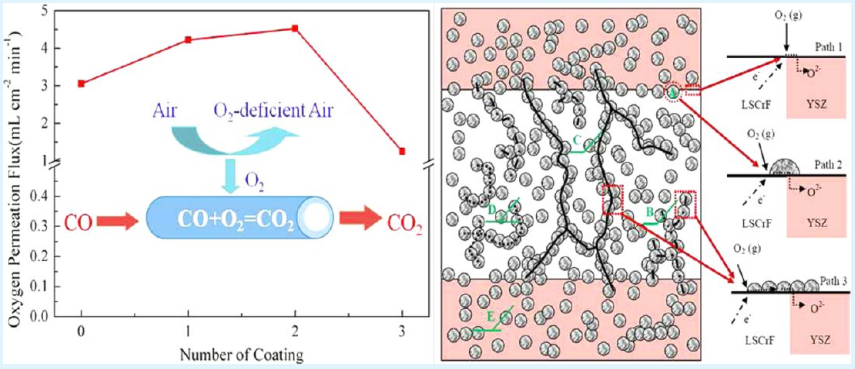

ABSTRACT: $Zr_{0.84}Y_{0.16}O_{1.92}$–$La_{0.8}Sr_{0.2}Cr_{0.5}Fe_{0.5}O_{3-\delta}$ (YSZ-LSCrF) dual-phase composite hollow fiber membranes were prepared by a combined phase-inversion and sintering method. The shell surface of the hollow fiber membrane was modified with $Ce_{0.8}Sm_{0.2}O_{1.9}$ (SDC) via a drop–coating method. As the rate of oxygen permeation of the unmodified membrane is partly controlled by the surface exchange kinetics, coating of a porous layer of SDC on the shell side (oxygen reduction side) of the hollow fiber membrane was found to improve its oxygen permeability. Rate enhancements up to 113 and 48% were observed, yielding a maximum oxygen flux of 0.32 and 4.53 mL min^{-1} cm^{-2} under air/helium and air/CO gradients at 950 °C, respectively. Excess coating of SDC was found to induce significant gas phase transport limitations and hence lower the rate of oxygen permeation. A model was proposed to calculate the length of triple phase boundaries (TPBs) for the coated dual-phase composite membrane and to explain the effect of coating on the oxygen permeability.

KEYWORDS: *surface modification, oxygen separation membrane, samaria-doped ceria, dual-phase composite, triple-phase boundary, hollow fiber*

INTRODUCTION

In recent years, dense ceramic membranes exhibiting high oxygen ionic and electronic conductivity have attracted increasing attention as a potentially economic, clean, and efficient means of producing oxygen by separation from air.[1−4] One of the challenging applications concerns their use in membrane reactors for natural gas conversion to syngas.[5−9] It is expected that membrane-based production of syngas can reduce the costs considerably.[10]

To date, oxygen-deficient mixed ionic–electronic conducting perovskite type oxides such as $(Ln,A)(Co,Fe)O_{3-\delta}$ (Ln = rare earth; A = Sr, Ba) are studied most intensively.[1−4] The cobalt-containing perovskites possess high oxygen permeability, but their long-term structural stability remains an issue of ongoing concern.[11−14] The cobalt may be replaced as a whole by a less reducible transition metal such as chromium, but then the resulting permeability becomes rather poorer,[15,16] That is, the improvement of the stability occurs at the expense of the oxygen flux. An alternative approach involves the preparation of a dual–phase membrane by dispersion of a stable perovskite phase composition, lacking a high intrinsic oxide ionic conductivity, into a solid oxide electrolyte.[17−19] Both phases need to be continuous to provide efficient pathways for both ionic and electronic transport.

Oxygen permeation process involves exchange of oxygen between the gas phase and the membrane surfaces and transport of oxide ions and electrons in the bulk of the membranes.[1,2] When the membrane is thick, the overall process

Received: June 2, 2013
Accepted: September 10, 2013
Published: September 10, 2013

is likely limited by the bulk transport. In this case, reducing the thickness will result in increased oxygen permeation flux. But, when the membrane becomes thinner than a certain value, no significant gain in flux can be achieved by further reducing the thickness, because the overall process is then controlled by the surface exchange. To enhance the surface exchange and thus the overall permeation process,[20−26] one can consider applying catalyst to the membrane surfaces, e.g., via dip coating or screen printing. For promoting the surface oxygen exchange at the feed side of the membrane, the catalysts can be chosen from perovskite-type mixed oxygen ionic and electronic conductors, e.g., $La_{1-x}Sr_xCoO_{3-\delta}$ (LSC), $La_{0.6}Sr_{0.4}Co_{0.8}Fe_{0.2}O_{3-\delta}$ (LSCF6482) and $Ba_{1-x}Sr_xCo_{1-y}Fe_yO_{3-\delta}$ (BSCF), which are also considered as potential cathode material in the intermediate−temperature solid oxide fuel cell (IT−SOFC). The earth-alkaline containing cobalt-based perovskite-type oxides, however, suffer a poor stability in CO_2−containing atmospheres.[11−14] Recently, Wang et al. reported significant enhancement of the surface exchange kinetics of perovskite-type oxides $La_{0.8}Sr_{0.2}MnO_{3-\delta}$ and $Sr_2Fe_{1.5}Mo_{0.5}O_6$ by surface coating with solid oxide electrolytes such as yttria-stabilized zirconia (YSZ) and samarium-doped ceria (SDC).[27,28] Some larger enhancement was found for SDC. Even coating of SDC on the known mixed conductor like LSCF6482 was found to improve the surface exchange rate.[29] The enhanced surface exchange kinetics relative to that exhibited by the unmodified perovskite-type phase was attributed by the authors to spill over of oxygen atoms (formed by oxygen dissociative adsorption) onto the electrolyte surface, followed by fast incorporation in the oxide electrolyte and, subsequently, into the perovskite-type phase.[27−29]

In previous research, we have demonstrated that the dual-phase hollow fiber membranes consisting of YSZ and $La_{0.8}Sr_{0.2}Cr_{0.5}Fe_{0.5}O_{3-\delta}$ (LSCrF) meet the stability requirements for use in membrane reactors for partial oxidation of methane.[5,18] Because the hollow fiber membrane had a relatively small thickness (~0.3 mm), it is likely that the overall oxygen permeation process was at least partly limited by the surface oxygen exchange. In this study, we explored the effect of surface modification of the shell side (oxygen reduction side) of the hollow fiber membranes with 20 mol % samarium-doped ceria ($Ce_{0.8}Sm_{0.2}O_{1.9}$, SDC) by means of oxygen permeation flux measurements under both air/helium and air/CO gradients. A model for calculating the geometrical triple-phase-boundary (TPB) length has been applied for interpretation of the experimental data.

EXPERIMENTAL DETAILS

2.1. Preparation of Dual-Phase Hollow Fiber Membranes. YSZ−LSCrF dual-phase hollow fiber membranes were prepared using a combined phase-inversion and sintering technique.[5,6,9,13,17,18] The LSCrF powder was synthesized via a conventional solid state reaction route. Appropriate amounts of La_2O_3 (AR, Sinopharm Chemical Reagent Co., China), $SrCO_3$ (AR, Sinopharm Chemical Reagent Co., China), Cr_2O_3 (AR, Sinopharm Chemical Reagent Co., China), and Fe_2O_3 (AR, Sinopharm Chemical Reagent Co., China) were weighed and ball-milled, then calcined at 1200 °C for 10 h to yield perovskite LSCrF powder. YSZ was a commercial powder (> 99 %, Fanmeiya Co., China).The starting suspension consisted of 43.59 wt % YSZ powder and 32.04 wt % LSCrF powder, 20.17 wt % N−methyl−2-pyrrolidone (NMP) (CP, Sinopharm Chemical Reagent Co., China) as solvent, 3.36 wt % polyethersulfone (PESf) (Radel A−100, Solvay Advanced Polymers, USA) as binder, and 0.84 wt % polyvinylpyrrolidone (PVP) (K30, CP, Sinopharm Chemical Reagent Co., China) as dispersant; the amounts of YSZ and LSCrF used here correspond to a volume ratio of 60/40 in the final sintered product. The suspension was stirred for 48 h and degassed for two hours, then extruded through a tube−in-orifice spinneret (outer diameter 2.6 mm, inner diameter 1.2 mm) using nitrogen (three bar). The hollow fiber emerging from the spinneret passed through an air gap (1.0 cm) and was immersed in a water bath to complete solidification. The internal water injection rate was 4 m min^{-1}. After desiccation for 48 h, the fiber was sintered at 1450 °C for 10 h in air.

The shell side of the sintered YSZ-LSCrF hollow fiber membrane was coated with nanoparticles of SDC by means of drop-coating. The aqueous solution used for coating was prepared from $Ce(NO_3)_3$ and $Sm(NO_3)_3$ in the appropriate molar ratio and with a total metal ion concentration of about 0.1M. The coated membrane was dried under an infrared light and subsequently fired at 1000 °C for 1 h. Samples with different SDC loadings were obtained by repeating this procedure. The mass increase of 0.30−0.50 mg m^{-2} for one cycle was measured by an electronic precision balance (AB135-S, Mettler-Toledo Inc, Swiss) before and after coating and subsequent annealing. The microstructure and composition of the SDC-coated hollow fiber membranes were examined using scanning electron microscopy (SEM, SIRION200, FEI, USA) and energy-dispersive X-ray spectroscopy (EDX, Oxford INCA, UK).

2.2. Oxygen Permeation Measurements. A permeation cell was constructed by joining two ends of a 44.60 mm long hollow fiber membrane to two Al_2O_3 tubes using a glass sealant at 1020 °C. The shell side of the hollow fiber was exposed to ambient air, and the lumen side was swept with either CO or helium (He) both at a rate of 30 mL min^{-1}. The effluent gas was analyzed by a dual column gas chromatograph (GC-14C, Shimadazu, Japan and GC9750, FuLi, China) equipped with a thermal conductivity detector, in which O_2, N_2, and CO was separated by 60−80 mesh 5 Å molecular sieve column and CO_2 by 60−80 mesh GDX-502 column. Because of imperfection in the glass sealant or the membrane, some oxygen may leak from the shell into the lumen side. The extent of the oxygen leakage was monitored by measuring the nitrogen concentration in the effluent. In this study, the leaked oxygen accounted for less than 1% of the oxygen passing through the membranes under air/helium gradient, and much less under air/CO gradient. The oxygen permeation flux was calculated from the oxygen or CO_2 concentration and flow rate of the effluent, and corrected for the oxygen leakage. The as-determined oxygen permeation flux was normalized to the average surface of the hollow fiber $S = 2\pi (r_{outer}\text{-}r_{inner})L/\ln(r_{outer} / r_{inner})$,[30] in which L, r_{outer}, r_{inner} are the length, outer, and inner radius of the hollow fiber, respectively.

RESULTS

3.1. Membrane Preparation and Morphology. Figure 1 shows backscattered electron SEM micrographs of an YSZ−LSCrF dual-phase hollow fiber sintered in air at 1450°C for 10 h. The as-prepared hollow fiber membrane had an outer diameter of 1.80 mm and wall thickness of 0.27 mm. It consisted of a thick dense layer sandwiched by two thin porous layers of finger-like voids (Figure 1A). The finger-like voids at the lumen side grow significantly deeper than those at the shell side. It has been shown that formation of the finger-like voids in hollow fibers is strongly influenced by the viscosity of the ceramic suspension during the phase-inversion stage.[31,32] Because of the presence of the air-gap, the shell side surface of the hollow fiber was exposed to the ambient atmosphere before immersion into water bath, while the lumen side surface of the hollow fiber was immediately brought into contact with flowing water. This led to the evaporation of solvent NMP at the shell side and diffusion of the solvent from the shell to the lumen side. Consequently, the viscosity of the hollow fiber at the shell side became higher than that at the lumen side,

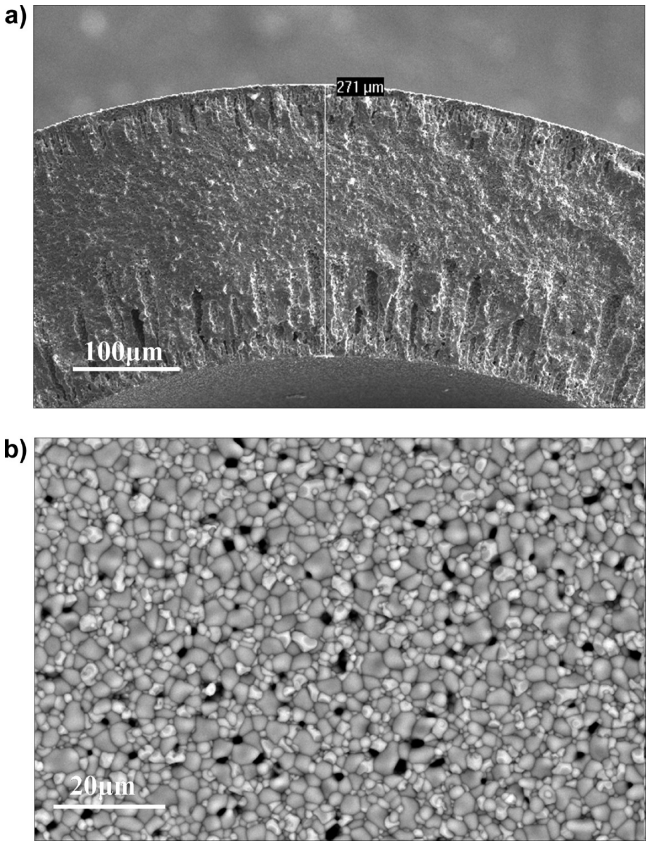

Figure 1. Images of the as-prepared YSZ−LSCrF dual-phase composite hollow fiber membrane. (A) SEM image of cross-section, (B) BSE image of shell surface.

thereby causing a significant difference in penetration depth of the fingerlike voids between the two sides.

The sintered hollow fiber was comprised of YSZ and LSCrF as major phases. In Figure 1B, the bright, gray and dark regions correspond to the LSCrF, YSZ and pores, respectively. The mean grain sizes for the LSCrF and YSZ phases were calculated to be ∼2 and ∼1 μm, respectively. And the total TPB length per unit area was estimated to be 0.32 μm μm^{-2} using the Otsu method.[33]

The drop-coating procedure turned out to be effective for the deposition of SDC nanoparticles on the shell side of YSZ-LSCrF hollow fiber membranes. Figure 2A−C shows typical SEM micrographs of the surface coated with 0.51, 0.93, and 1.31 mg cm^{-2} SDC, respectively. At the lowest loading of 0.51 mg cm^{-2}, SDC did not form a uniform layer. The coverage increased with increasing the number of deposition cycles (coating, drying, and annealing). The presence of pores in the coated layer is desirable as it can facilitate the transport of gaseous oxygen through the layer. When the SDC loading was increased to the maximum value in this study of 1.31 mg cm^{-2}, the surface was almost completely covered with SDC. From the inserted SEM image in Figure 2C, the size of SDC nanoparticle was determined to be in the range from 25 to 75 nm. The thickness of the corresponding layer was estimated to be ∼2.0 μm from the cross−sectional SEM image (Figure 2D). An EDX analysis on the whole area shown in Figure 2C revealed that the SDC layer had a composition similar to that reported in literature.[34]

The degree of the membrane surface covered by the SDC particles, θ_{SDC}, can be estimated using the equation

$$\theta_{SDC} = \frac{m}{\rho S d} \quad (1)$$

where m is the SDC loading, ρ the density of SDC oxide (7.148 g cm^{-3}) (JSPCD, No. 75−0158), S the outer surface area of the hollow fiber, d the thickness of the SDC layer (∼2 μm). Thus, the SDC loadings of 0.51, 0.93, and 1.31 mg cm^{-2} correspond to the SDC coverage degrees of 35, 64, and 91%, respectively.

3.2. Oxygen Permeation Properties. Figure 3 shows the effect of SDC deposition loading on the oxygen permeation rate of the dual-phase YSZ−LSCrF hollow fiber membrane under air/He and air/CO gradients at 950 °C. Clearly, the oxygen flux was enhanced by the deposition of SDC on the shell surface of the hollow fiber membrane. The oxygen flux reached maximum after two deposition cycles, which corresponded to a SDC loading of 0.93 mg cm^{-2}. At 950 °C, the maximum oxygen fluxes were 0.32 and 4.53 mL min^{-1} cm^{-2} (STP) (equivalent to 2.47×10^{-7} and 3.37×10^{-6} mol s^{-1} cm^{-2}) under air/He and air/CO gradient, which were about 113 and 48% higher than that for the uncoated membrane, respectively. A lowering of the oxygen flux was observed when the SDC coverage was further increased to 1.31 mg cm^{-2}.

Arrhenius plots of the oxygen fluxes under air/CO gradients are shown in Figure 4. Small differences were found in the apparent activation energies obtained after one and two SDC deposition cycles relative to that observed for the uncoated membrane. A profound increase of the apparent activation energy was found, from about 100 kJ mol^{-1} after two deposition cycles to a value of 156 ± 2 kJ mol^{-1} after three deposition cycles.

Higher oxygen permeation flux means higher surface oxygen exchange rate and k_{chem}. When 0.93 mg·cm^{-2} SDC materials were introduced, the surface exchange on hollow fiber membrane was the fastest, and the largest (optimized) oxygen permeation fluxes of 0.32 mL·min^{-1}·cm^{-2} under air/He gradient at 950 °C and 1.79, 3.04, and 4.53 mL min^{-1} cm^{-2} under air/CO gradient at the temperature of 850−950 °C were obtained.

It is also noticed that during the oxygen permeation measurements, the hollow fiber membrane experienced four−times cooling down to room temperature and reheating up to 1000 °C at a temperature step of 3 °C min^{-1}, and no cracks of hollow fiber and SDC coating layer were observed, indicating good heat-shock resistance of the fiber and the SDC coating.

DISCUSSION

Oxygen permeation through a dense ceramic membrane consists of exchange of oxygen between the gas phase and the surface of the solid and counter diffusion of oxide ions and electrons in the bulk.[1,2] In the case that the overall oxygen permeation process is limited partly or even completely by the surface oxygen exchange step, modifying the membrane surface could lead to the increase in oxygen permeation flux. It was shown in the present study that for the dual-phase composite membrane constituting YSZ as an oxygen ionic conductor and LSCrF as an electronic conductor, the oxygen permeation was enhanced through coating the membrane surface with another oxygen ionic conductor SDC. This indicates that the overall oxygen permeation process for the bare YSZ−LSCrF membrane was limited by the surface oxygen exchange step to some extent, and the limitation could be alleviated by coating with SDC nanoparticles.

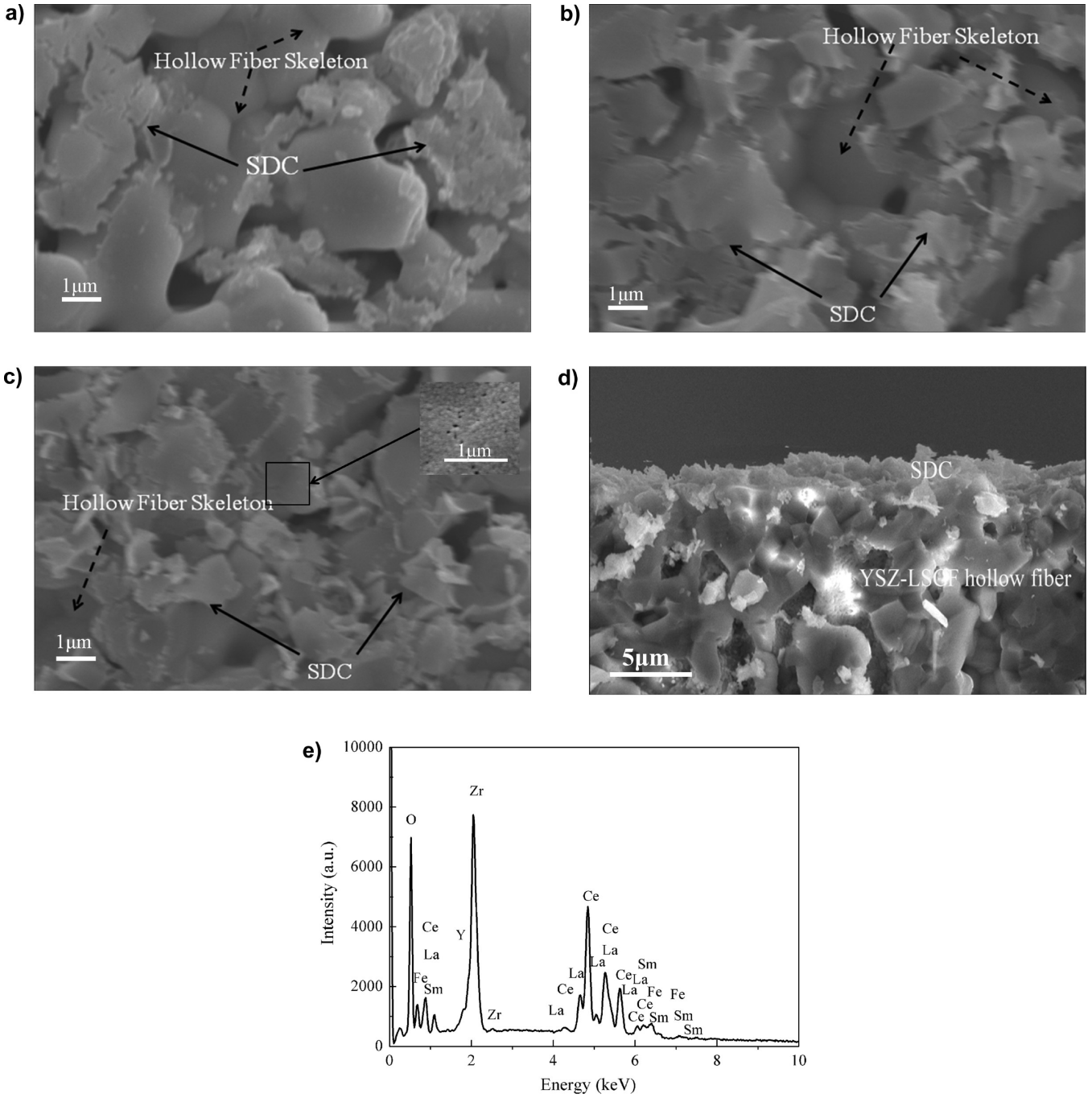

Figure 2. SEM images and EDX analysis of the YSZ−LSCrF dual−phase composite hollow fiber membrane with different SDC loadings. (A) 0.51 mg cm^{-2} SDC (1−time coating), (B) 0.93 mg cm^{-2} SDC (2−times loading), (C) 1.31 mg cm^{-2} SDC (3−times loading), (D) SDC/YSZ−LSCrF interface, (E) EDX profile of C.

To explain the positive effect of the SDC coating on the surface oxygen exchange, a mechanism is proposed, as schematically illustrated in Figure 5. The SDC particles on the YSZ−LSCrF shell side surface are assumed to be randomly distributed. Some particles, labeled as A in Figure 5, are located at the boundaries of YSZ and LSCrF. And some particles labeled as B and C constitute continuous networks that are connected to the YSZ−LSCrF boundaries. The TPBs constituting these SDC nanoparticles are active for oxygen reduction. But, some SDC nanoparticles, labeled as D, are not linked to the YSZ/LSCrF boundaries, thus they are not active for oxygen reduction, because the oxide ions produced at the TPBs can not migrate to the YSZ/LSCrF boundaries and incorporate into the YSZ phase. SDC nanoparticles located on the surface of YSZ grains (labeled as E) are also not active, because electrons required for oxygen reduction is not available.

On the basis the proposed reaction and transport schemes, a model originally proposed for SDC-coated single-phase perovsikite-based electrodes in solid oxide fuel cells,[35−37] is adopted to calculate the probabilities of SDC nanoparticles belonging to types A, B, C, and the corresponding TPB length.

The probability of type C particles, p_C, is calculated from

dx.doi.org/10.1021/am402125j | ACS Appl. Mater. Interfaces 2013, 5, 9454−9460

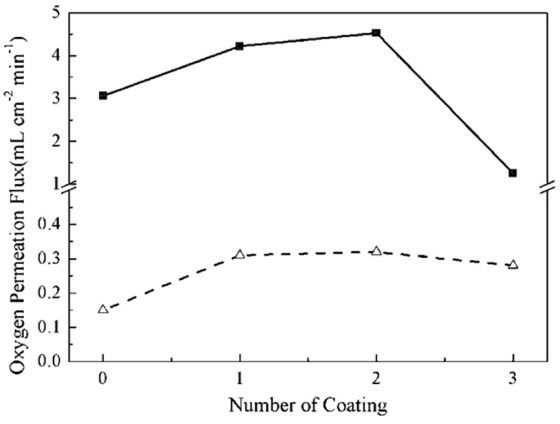

Figure 3. Effect of SDC loading on oxygen permeation fluxes through the YSZ−LSCrF composite hollow fiber membrane at 950 °C. (Δ) under air/He gradient, (■) under air/CO gradient. Membrane dimension: length 44.60 mm, outer diameter 1.80 mm, wall thickness 0.27 mm.

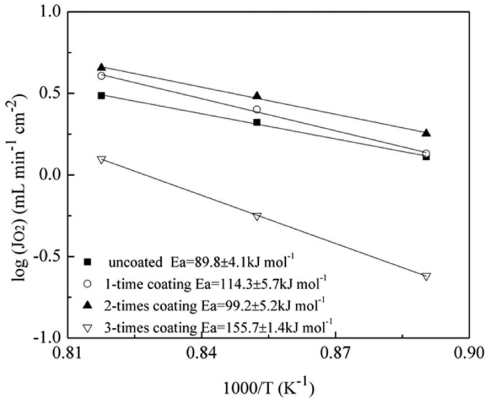

Figure 4. Temperature dependence of oxygen permeation fluxes through the YSZ−LSCrF composite hollow fiber membrane with different SDC loadings under air/CO gradient. (■) uncoated sample, (○) 0.51 mg cm^{-2} SDC (1-time coating), (▲) 0.93 mg cm^{-2} SDC (2-times loading), (▽) 1.31 mg cm^{-2} SDC (3-times loading). Membrane dimension: length 44.60 mm, outer diameter 1.80 mm, wall thickness 0.27 mm.

$$p_C = \left[1 - \left(\frac{4.236 - Z}{2.472}\right)^{2.5}\right]^{0.4} \quad (2)$$

where Z is the coordination number of contacts between the SDC particles, which in turn is determined from

$$Z = \bar{Z}\frac{\theta_{SDC}/r_{SDC}}{\theta_{SDC}/r_{SDC} + \theta_{pore}/r_{pore}} \quad (3)$$

where $\bar{z}$ is the average coordination number of all particles, θ_{pore} the porosity of the SDC layer, r_{pore} and r_{SDC} are the radius of pores and SDC nanoparticles, respectively. Note that $\theta_{SDC} + \theta_{pore} = 1$.

The probability of type B particles, p_B, is calculated from

$$p_B = \sum_{i=2}^{N}(1 - p_C)\left[2.807\frac{Z}{\bar{Z}}(1 - p_C)^{0.4}\right]^{1.572(i-1)} \quad (4)$$

where i represents the ith row of the SDC nanoparticles and N is the total number of the rows, which is equal to the ratio of the size of LSCrF grains to the size of SDC nanoparticles.

The probability of type A particles located on the LSCrF/YSZ grain boundaries, p_A, is readily available, for it holds that $p_A + p_B + p_C = 1$.

The TPB length corresponding to Path 1, in Figure 5, L^1_{TPBs}, can be calculated from

$$L^1_{TPBs} = L_{TPBs,0}(1 - \theta_{SDC}) \quad (5)$$

where $L_{TPBs,0}$ is the original effective TPBs length per unit area.

The TPB length corresponding to the Path 2, L^2_{TPBs}, is

$$L^2_{TPBs} = L_{TPBs,0}\theta_{SDC}\pi p_A \quad (6)$$

And the TPB length, corresponding to the Path 3, L^3_{TPBs}, is

$$L^3_{TPBs} = 3\sin\theta_{SDC,LSCrF}\frac{\theta_{pore}\theta_{SDC}}{r_{SDC}}(p_B + p_C)V_{LSCrF} \quad (7)$$

where $\theta_{SDC,LSCrF}$ is the contact angle between SDC nanoparticles and LSCrF grains and V_{LSCrF} is the phase volume fraction of LSCrF in the composite.

The total TPB length (L_{TPBs}) for the SDC-coated YSZ−LSCrF composite can thus be obtained by summation of L^1_{TPBs}, L^2_{TPBs}, and L^3_{TPBs}. For sake of the simplicity of calculation, the size of SDC nanoparticles is assumed to be equal to the size of pores between the SDC nanoparticles, and the contact angle of SDC nanoparticles with LSCrF grains is set as 90 °.

Figure 6 shows the as-calculated TPBs length as a function of the SDC surface coverage. Since the SDC nanoparticle size ranged from 25 to 75 nm, the TPB length was calculated for three different sizes: 25, 50, and 75 nm. It can be seen that initially the TPBs length increases linearly with increasing θ_{SDC}. It is because that at low θ_{SDC}, the increased TPB length mainly arises from the SDC nanoparticles sitting at the boundaries of YSZ/LSCrF (labeled as A in Figure 5). When θ_{SDC} exceeds a certain value, ~30 % in the present case, with further increasing θ_{SDC}, TPB increases rapidly, reaches a maximum at θ_{SDC} of ~55 %, and decreases till zero at full coverage. This complicated dependence of TPB length on θ_{SDC} can be explained as follows. When θ_{SDC} exceeds a certain value, SDC nanoparticles start to form percolated networks, leading to the increase of TPB length. But, increasing the SDC coverage (θ_{SDC}) is at the expense of the volume fraction of pores (θ_{pore}), resulting in a decrease of TPB length. Because of the competition of above−described two competing processes, an optimal coverage occurs corresponding to the maximum for TPB length.

The variation of the TPB length with SDC coverage (Figure 6) generally matches with the variation of oxygen permeation (Figure 3). Clearly, the larger the TPB length, the higher the oxygen permeation rate is. But, there is no proportional linear relationship between them. One plausible explanation for this is given as follows. The oxide ions produced at the TPBs need to migrate over a distance through the SDC network to the YSZ/LSCrF boundaries before incorporation into the YSZ grains (see Path 3, Figure 5).[38] Therefore, the effectiveness of the TPBs is related to their distance to the YSZ/LSCrF boundaries: the SDC nanoparticles sitting at the YSZ/LSCrF boundaries are most effective, whereas the SDC nanoparticles sitting at the tails of the network are least effective.

Although a quantitative relationship between coating and the resulting oxygen permeation rate remains to be developed which is left to the future study, the proposed mechanism nevertheless can help identifying strategies to enhance the surface oxygen exchange and thus the oxygen permeation rate. To maximize the TPB length, appropriate amount of the

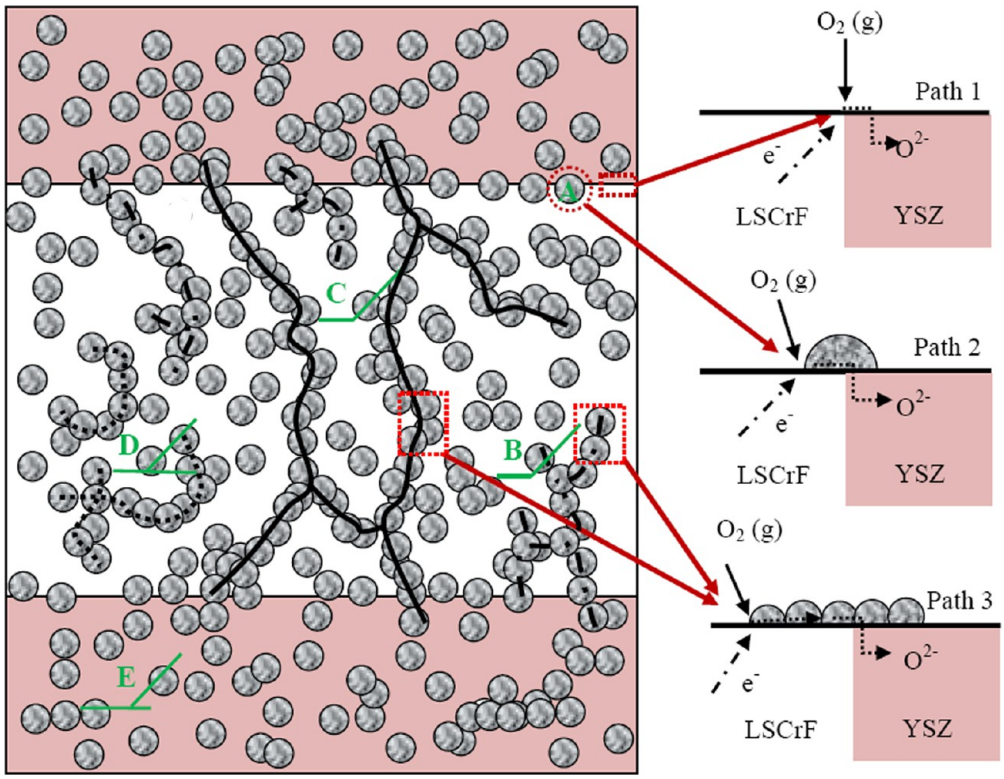

Figure 5. Schematic diagram of SDC-coated YSZ–LSCrF membrane.

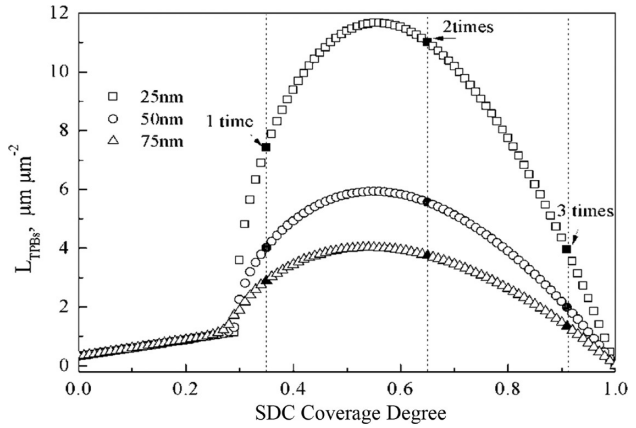

Figure 6. TPBs length in unit area, L_{TPBs}, as functions of SDC coverage degree θ_{SDC} and particle size r_i. $r_i = r_j$ = 25, 50, and 75 nm, $\theta_{SDC,LSCrF}$ = 90°. (■□) 25 nm, (○●) 50 nm, (▲△) 75 nm.

coating particle should be used. Note that as shown in eq 7, the TPB length associated with type B and C particles, L^3_{TPBs}, is inversely proportional to the radius of SDC nanoparticles (r_{SDC}). Thus, to increase the TPB length, the coating particle should be as small as possible. In the present case, it is shown in Figure 6 that reducing the SDC particle size from 75 nm to 25 nm results in increase of TPB length by about three times. And to reduce the diffusion distance of oxide ions, the grain size of the electron-conducting phase in the dual-phase composite membrane should be small. Moreover, the coating particles are preferred to have high concentration of mobile oxygen vacancies V_O in its surface layer, because the oxygen reduction ($O_2(g) + 2V_o + 4e^- = 2O_o^{2-}$) involves V_O, in addition to electronic species e^-. Because the as-produced oxide ions needs to transport through the coating materials before incorporation into the bulk of oxygen ion conducting phase of the composite, the coating particles are required to possess high oxygen ionic conductivity.

CONCLUSION

Shell surface of YSZ-LSCrF dual-phase composite hollow fiber membrane was modified by SDC using drop-coating method. The modified hollow fiber coated with different SDC loadings exhibits novel oxygen permeation properties and can be applied for membrane reactor. With the optimized SDC loading, the composite membrane has demonstrated the oxygen permeation flux of 0.32 and 4.53 mL min^{-1} cm^{-2} under air/He and air/CO gradient at 950 °C, respectively, which is larger than those of uncoated membrane, suggesting that surface modification with SDC is very promising for oxygen permeation process. A model was adopted to calculate the active TPBs length for the SDC-coated dual-phase composite, providing an explanation to the effect of the SDC coating on the oxygen permeation.

AUTHOR INFORMATION

Corresponding Authors

*E-mail: ccsm@ustc.edu.cn. Tel: +86-551-63600088. Fax: +86-551-63601760.

*E-mail: h.j.m.bouwmeester@tnw.utwente.nl. Tel: +31-53-4892202.

Notes

The authors declare no competing financial interest.

ACKNOWLEDGMENTS

This research was supported by National Natural Science Foundation of China (Grants 21076205, 21176230).

REFERENCES

(1) Bouwmeester, H. J. M.; Burggraaf, A. J. Dense ceramic membranes for oxygen separation. In *Fundamentals of Inorganic Membrane Science and Technology*; Burggraaf, A. J., Cot, L., Eds.; Membrane Science Technology Series; Elsevier: Amsterdam, 1996; Vol. *4*, Chapter 10 , pp 435−−528

(2) Sunarso, J.; Baumann, S.; Serra, J. M.; Meulenberg, W. A.; Liu, S.; Lin, Y. S.; da Costa, J. C. D. *J. Membr. Sci.* **2008**, *320*, 13−41.

(3) Liu, Y.; Tan, X.; Li, K. *Catal. Rev.* **2006**, *48*, 145−198.

(4) Teraoka, Y.; Zhang, H. M.; Furukawa, S.; Yamazoe, N. *Chem. Lett.* **1985**, *11*, 1743−1746.

(5) Liu, J. J.; Zhang, S. Q.; Wang, W. D.; Gao, J. F.; Liu, W.; Chen, C. S. *J. Power Sources* **2012**, *217*, 287−290.

(6) Caro, J.; Caspary, K. J.; Hamel, C.; Hoting, B.; Kolsch, P.; Langanke, B.; Nassauer, K.; Schiestel, T.; Schmidt, A.; Schomacker, R.; Seidel-Morgenstern, A.; Tsotsas, E.; Voigt, I.; Wang, H. H.; Warsitz, R.; Werth, S.; Wolf, A. *Ind. Eng. Chem. Res.* **2007**, *46*, 2286−2294.

(7) Balachandran, U.; Dusek, J.; Mieville, R. a.; Poeppel, R.; Kleefisch, M.; Pei, S.; Kobylinski, T.; Udovich, C.; Bose, A. *Appl. Catal. A* **1995**, *133*, 19−29.

(8) Tsai, C. Y.; Dixon, A. G.; Moser, W. R.; Ma, Y. H. *AIChE J.* **1997**, *43*, 2741−2750.

(9) Wu, Z. T.; Wang, B.; Li, K. *J. Membr. Sci.* **2010**, *352*, 63−70.

(10) Bharadwaj, S.; Schmidt, L. *Fuel Process Technol.* **1995**, *42*, 109−127.

(11) Yi, J.; Feng, S.; Zuo, Y.; Liu, W.; Chen, C. *Chem. Mater.* **2005**, *17*, 5856−5861.

(12) Shao, Z. P.; Yang, W. S.; Cong, Y.; Dong, H.; Tong, J. H.; Xiong, G. X. *J. Membrane Sci.* **2000**, *172*, 177−188.

(13) Li, J. L.; Zeng, Q.; Liu, T.; Chen, C. S. *Sep. Purif. Technol.* **2011**, *77*, 76−79.

(14) Yi, J.; Schroeder, M.; Weirich, T.; Mayer, J. *Chem. Mater.* **2010**, *22*, 6246−6253.

(15) Kruidhof, H.; Bouwmeester, H. J. M.; Vondoorn, R. H. E.; Burggraaf, A. J. *Solid State Ionics* **1993**, *63-5*, 816−822.

(16) Kharton, V.; Kovalevsky, A.; Tikhonovich, V.; Naumovich, E.; Viskup, A. *Solid State Ionics* **1998**, *110*, 53−60.

(17) Li, W.; Liu, J. J.; Chen, C. S. *J. Membrane Sci.* **2009**, *340*, 266−271.

(18) Liu, J. J.; Liu, T.; Wang, W. D.; Gao, J. F.; Chen, C. S. *J. Membr. Sci.* **2012**, *389*, 435−440.

(19) Kharton, V.; Kovalevsky, A.; Viskup, A.; Figueiredo, F.; Yaremchenko, A.; Naumovich, E.; Marques, F. *J. Electrochem. Soc.* **2000**, *147*, 2814−2821.

(20) Tan, X. Y.; Wang, Z. G.; Liu, H.; Liu, S. M. *J. Membr. Sci.* **2008**, *324*, 128−135.

(21) Chen, Z. H.; Ran, R.; Shao, Z. P.; Yu, H.; da Costa, J. C. D.; Liu, S. M. *Ceram. Int.* **2009**, *35*, 2455−2461.

(22) Lee, S.; Lee, K. S.; Woo, S. K.; Kim, J. W.; Ishihara, T.; Kim, D. K. *Solid State Ionics* **2003**, *158*, 287−296.

(23) Lee, S.; Yu, J. H.; Seo, D. W.; Woo, S. K. *J. Electroceram.* **2006**, *17*, 719−722.

(24) Cheng, H. W.; Liu, J. H.; Lu, X. G.; Ding, W. Z. *ACS Appl. Mater. Interfaces* **2011**, *3*, 4032−4039.

(25) Liu, H.; Tan, X. Y.; Pang, Z. B.; da Costa, J. C. D.; Lu, G. Q.; Liu, S. M. *Sep. Purif. Technol.* **2008**, *63*, 243−247.

(26) Kida, T.; Ninomiya, S.; Watanabe, K.; Yamazoe, N.; Shimanoe, K. *ACS Appl. Mater. Interfaces* **2010**, *2*, 2849−2853.

(27) Wang, Y.; Zhang, L.; Xia, C. R. *Int. J. Hydrogen Energy* **2012**, *37*, 2182−2186.

(28) Zhang, L.; Liu, Y. Q.; Zhang, Y. X.; Xiao, G. L.; Chen, F. L.; Xia, C. R. *Electrochem. Commun.* **2011**, *13*, 711−713.

(29) Hong, T.; Zhang, L.; Chen, F. L.; Xia, C. R. *J. Power Sources* **2012**, *218*, 254−260.

(30) Rathore, M. M. *Thermal Engineering*; McGraw-Hill Education: New York, 2010; p 1033.

(31) Kingsbury, B. F. K.; Li, K. *J. Membr. Sci.* **2009**, *328*, 134−140.

(32) Jin, C.; Yang, C. H.; Chen, F. L. *J. Membr. Sci.* **2010**, *363*, 250−255.

(33) Otsu, N. *Automatica* **1975**, *11*, 23−27.

(34) Jiang, S. P. *Int. J. Hydrogen Energy* **2012**, *37*, 449−470.

(35) Chen, D. F.; Lin, Z. J.; Zhu, H. Y.; Kee, R. J. *J. Power Sources* **2009**, *191*, 240−252.

(36) Zhang, Y. X.; Xia, C. R. *Electrochim. Acta.* **2011**, *56*, 4763−4769.

(37) Zhang, Y. X.; Wang, Y. L.; Wang, Y.; Chen, F. L.; Xia, C. R. *J. Power Sources* **2011**, *196*, 1983−1991.

(38) Adler, S. B. *Chem. Rev.* **2004**, *104*, 4791−4843.